Single-Atom Resolved Fluorescence Imaging of an Atomic Mott Insulator

Jacob F. Sherson[1][*][†], Christof Weitenberg[1][*], Manuel Endres[1], Marc Cheneau[1], Immanuel Bloch[1,2], and Stefan Kuhr[1][‡]

[1]*Max-Planck-Institut für Quantenoptik, Hans-Kopfermann-Str. 1, 85748 Garching, Germany*

[2]*Ludwig-Maximilians-Universität, Schellingstr. 4/II, 80799 München, Germany*

(Dated: 29 July 2010)

The reliable detection of single quantum particles has revolutionized the field of quantum optics and quantum information processing. For several years, researchers have aspired to extend such detection possibilities to larger scale strongly correlated quantum systems, in order to record in-situ images of a quantum fluid in which each underlying quantum particle is detected. Here we report on fluorescence imaging of strongly interacting bosonic Mott insulators in an optical lattice with single-atom and single-site resolution. From our images, we fully reconstruct the atom distribution on the lattice and identify individual excitations with high fidelity. A comparison of the radial density and variance distributions with theory provides a precise in-situ temperature and entropy measurement from single images. We observe Mott-insulating plateaus with near zero entropy and clearly resolve the high entropy rings separating them although their width is of the order of only a single lattice site. Furthermore, we show how a Mott insulator melts for increasing temperatures due to a proliferation of local defects. Our experiments open a new avenue for the manipulation and analysis of strongly interacting quantum gases on a lattice, as well as for quantum information processing with ultracold atoms. Using the high spatial resolution, it is now possible to directly address individual lattice sites. One could, e.g., introduce local perturbations or access regions of high entropy, a crucial requirement for the implementation of novel cooling schemes for atoms on a lattice.

Ultracold atoms in optical lattices have proven to be powerful simulators for the investigation of the static quantum phases and dynamical evolutions of strongly correlated quantum many-body systems. Prominent examples include the quantum phase transition from a superfluid to a Mott insulator [1–4] and the fermionized Tonks-Girardeau gas for bosonic particles [5, 6], as well as the recently realized fermionic Mott insulator [7, 8]. In all these cases, the strong interactions between the particles compared to their kinetic energy generate intriguing highly correlated quantum states that are of fundamental interest in condensed matter physics and promising for practical applications in quantum information science. For many of these applications it is of crucial importance to image the correlated many-body systems with single-atom and single-site resolution. One could then e.g. probe the evolution from a Poissonian atom number distribution into highly number squeezed Fock states on a lattice not only globally [9] but also on a local scale. Furthermore one should be able to directly observe critical phenomena in the in-situ density or in spin-resolved images of the particles when approaching a quantum critical point. For applications in quantum information science, it is essential to address and manipulate single atoms on individual lattice sites. A prominent example is the one-way quantum computer [10] where local single particle measurements and operations are carried out after a successful global entanglement operation that creates
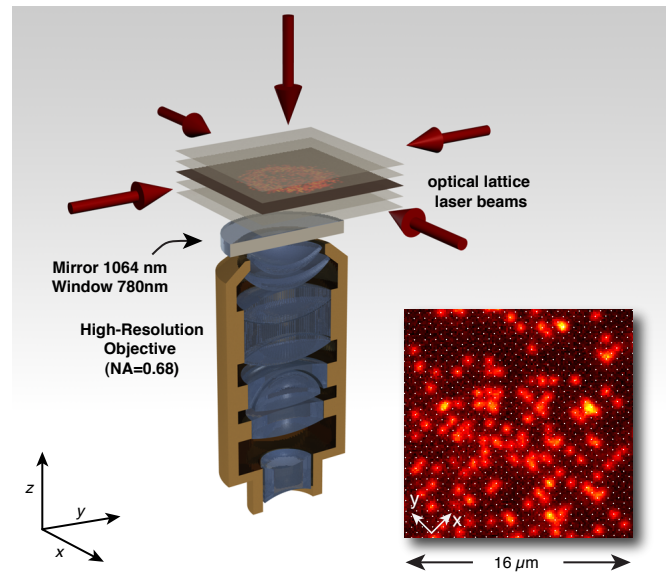

FIG. 1: **Experimental Setup.** Two-dimensional bosonic quantum gases are prepared in a single 2D plane of an optical standing wave along the $z-$direction, which is created by retroreflecting a laser beam ($\lambda = 1064\,\text{nm}$) on the coated vacuum window. Additional lattice beams along the x- and y-directions are used to bring the system into the strongly correlated regime of a Mott insulator. The atoms are detected using fluorescence imaging via a high resolution microscope objective. Fluorescence of the atoms was induced by illuminating the quantum gas with an optical molasses that simultaneously laser cools the atoms. The inset shows a section from a fluorescence picture of a dilute thermal cloud (points mark the lattice sites).

———————

[*] These authors contributed equally to this work.

[†] present address: Department of Physics and Astronomy, University of Aarhus, DK-8000 Aarhus C, Denmark.
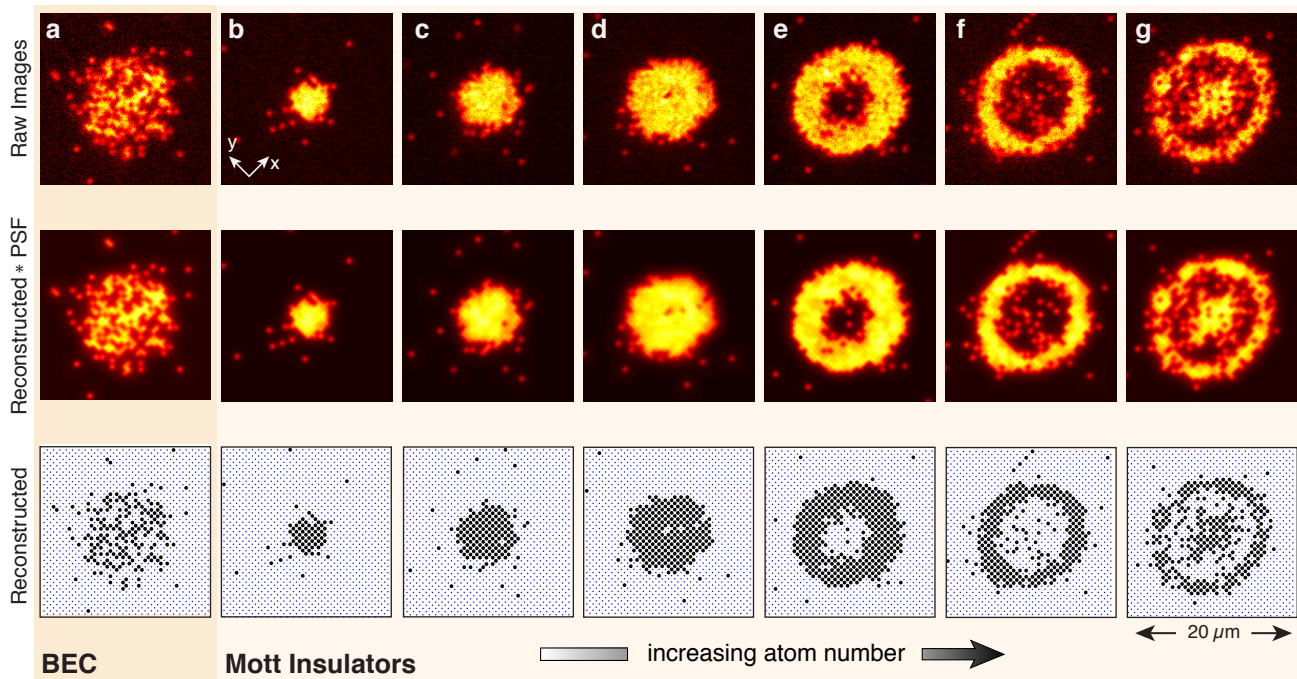
[‡] Electronic address: stefan.kuhr@mpq.mpg.de

FIG. 2: **High resolution fluorescence images of a BEC and Mott insulators.** Top row: Experimentally obtained images of a BEC **(a)** and Mott insulators for increasing particle numbers **(b-g)** in the zero-tunneling limit. Middle row: Numerically reconstructed atom distribution on the lattice. The images were convoluted with the point spread function of our imaging system for comparison with the original images. Bottom row: Reconstructed atom number distribution. Each circle indicates a single atom, the points mark the lattice sites. BEC and MIs were prepared with the same in-plane harmonic confinement (see Supplementary Information for the Bose-Hubbard model parameters of our system).

a highly-correlated cluster state.

Over the past years tremendous progress has been made in the high-resolution and single-atom sensitive detection of atoms on a lattice [11–15]. However, it has only now become possible to apply these techniques to the detection of strongly correlated quantum systems, in the work presented here and the work of Bakr et al. [16]. Here we report on in-situ fluorescence imaging of a Mott insulator (MI) with single-atom and single-site resolution. From a *single* image, we reconstruct the atom distribution on the lattice and individual thermal excitations of the MI become directly visible. This allows us to observe the number squeezing and the quality of an atomic Mott insulator down to a single lattice site. Using a simple model [17, 18] we characterize the average density distribution and number fluctuations of the quantum system, and use this for an in-situ temperature measurement. We find excellent agreement between our theory that assumes global thermal equilibrium. Furthermore, we show how the incompressible Mott phase evolves into a compressible normal phase as the temperature is increased.

Our experiments start with an almost pure 2D Bose-Einstein condensate [4] (BEC) of up to a few thousand ^{87}Rb atoms that was prepared in a single pancake-shaped antinode of a vertical optical standing wave (beam waist $w_0 = 75\,\mu$m) oriented along the z-axis (see Fig. 1). The

lattice depth was $V_z = 26(2)\,E_r$, where $E_r = h^2/(2m\lambda^2)$ is the recoil energy, m denotes the atomic mass of ^{87}Rb and λ the lattice wavelength. Additional beams along the x- and y-directions were used to load the 2D quantum gas into an optical lattice. All lattice beams had a wavelength $\lambda = 1064\,$nm resulting in a lattice period of $532\,$nm. We detected the atoms in the lattice by high-resolution fluorescence imaging through a specially designed microscope objective with a numerical aperture of NA $= 0.68$ and an optical resolution (FWHM) of $\approx 700\,$nm at a wavelength of $780\,$nm. For detection, the lattice depths along all three directions were increased to $V_{x,y,z}/k_B \approx 300\,\mu$K before an optical molasses induces fluorescence and simultaneously laser cooled the atoms [11, 15] (see Methods). In the low density thermal clouds (inset in Fig. 1) individual atoms are directly visible above an almost indiscernible background and their positions have a discrete spacing given by our lattice period (see Supplementary Information). During the imaging, atom pairs on a lattice site are immediately lost due to inelastic light-induced collisions [19]. We therefore only detect the particle number modulo two on each lattice site. This essentially amounts to recording the parity of the atom number.

The 2D lattice gases used in our experiments are well described by the Bose-Hubbard model, where particles are restricted to occupy the lowest energy band of the

lattice and their kinetic energy is characterized by a tunneling matrix element J and an on-site two-particle interaction energy U (see Refs. [20, 21]). For a BEC loaded into a weak lattice potential, $U/J \ll 1$, one expects a Poissonian atom number distribution on a lattice site i, as the classical coherent matter wave field of a BEC is characterized by Glauber's coherent states. Such states with an average filling of $\bar{n}_i$ per lattice site, exhibit a corresponding variance in the particle number $\sigma_i^2 = \bar{n}_i$. When the interactions between the particles relative to their kinetic energy are increased, the system undergoes a quantum phase transition to a Mott insulating state [1–3]. For homogeneous conditions and a 2D simple square lattice, this transition is expected to occur at $(U/J)_c \simeq 16.4$ (see Ref. [22]), where small shifts of this critical value have been reported when the system is additionally exposed to an underlying harmonic trapping potential [23]. In our case such an additional harmonic confinement was caused by the Gaussian beam profile of our lattice beams ($1/e^2$ waist of 75μm) and resulted in an in-plane harmonic confinement with trapping frequencies $\omega_x/(2\pi) = 72(4)$ Hz and $\omega_y/(2\pi) = 83(4)$ Hz for lattice depths of $V_{x,y} = 23(2) E_r$. For $U/J \gg (U/J)_c$ the atomic MI can be described by neglecting the tunneling energy of the system in the so called zero-tunneling approximation. The in-trap density distribution then exhibits a pronounced shell structure of incompressible regions where the density is pinned to integer values and increases in a step-like manner from the outer wings to the inner core [2, 13, 24, 25]. At zero temperature the particle number variance at a lattice site is then expected to vanish ($\sigma_i^2 = 0$) resulting in perfect Fock states. For low, but still finite temperatures $k_B T \ll U$, thermal fluctuations can be induced. These fluctuations limit the quality of the number squeezing and eventually lead to a complete melting of the characteristic shell structure of a MI when the temperature is increased above $T_m \simeq 0.2U/k_B$ (see Refs. [17, 18]).

We monitored the dramatic differences in the density profiles and the on-site number fluctuations by imaging the in-trap atom distributions of a BEC and a MI in the zero-tunneling limit for different atom numbers and temperatures (see Fig. 2, first row). For the MIs, the lattices along the x- and y-directions were increased in s-shaped ramps within 75 ms up to values of $V_{x,y} = 23(2) E_r$. To freeze out the atom distribution of a BEC, we ramped up the lattices within 0.1 ms. Using the point spread function (PSF) of our optical imaging system we were able to reconstruct the atom number distribution on the lattice with single-site and single-atom resolution via an image processing algorithm (see Methods). It works reliably even in the regions of high atomic density, as illustrated in Fig. 3.

To compare the digitally reconstructed atom distribution (see Fig. 2, bottom row) with the raw images, we show the reconstructed distribution convoluted with the PSF in the center row of Fig. 2. For a BEC with a Poissonian atom number distribution the average filling one
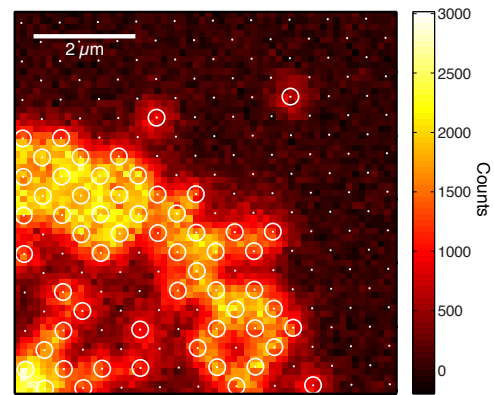

FIG. 3: **Identification of single atoms in a high-resolution image.** The points mark the centers of the lattice sites, circles indicate those sites where our deconvolution algorithm determined the presence of an atom. The image is a zoom into the upper right part of Fig. 2g.

detects due to the parity measurement in the fluorescence imaging is $\bar{n}_{i,\text{det}} = 1/2\left[1 - \exp\left(-2\bar{n}_i\right)\right]$, which saturates at $\bar{n}_{i,\text{det}} = 0.5$ for $\bar{n}_i \gtrsim 1.5$. In this limit, the detected atom number variance then saturates accordingly at $\sigma_{i,\text{det}}^2 = 0.25$. Indeed for a BEC, we observed that the recorded atomic density exhibits large atom number fluctuations from site to site. In contrast, for a MI we obtain plateaus of constant integer density, with almost vanishing fluctuations. For increasing particle numbers, the images in Fig. 2 show how successive MI shells are formed, which appear as alternating rings of one and zero atoms per site due to our parity measurement. In both the raw images and the reconstructed ones, individual defects are directly visible. The high symmetry of our atom clouds reflects the high optical quality of our lattice potentials. A small ellipticity is caused by the different harmonic trapping frequencies ω_x and ω_y.

We used the reconstructed site occupation numbers to determine the temperature of the sample based on a single image. For deep lattices, $U/J \simeq 300$, as used in our experiments for MIs, tunneling becomes completely suppressed such that coherent particle-hole fluctuations are expected to be negligible and defects are only induced by thermal fluctuations. The symmetry of our clouds allowed us to average the data azimuthally, taking into account the ellipticity, and to obtain radial profiles for the average density $\bar{n}_{\text{det}}(r)$ and variance $\sigma_{\text{det}}^2(r)$ (see Fig. 4a,b and Methods). We fitted analytic expressions derived in the zero-tunneling regime (see Methods) to our data. The results of such a fit for an $n = 1$ ($0 < \mu/U < 1$) and an $n = 2$ ($1 < \mu/U < 2$) MI are displayed in Fig. 4a,b. The MI regions can be identified as connected regions of constant integer density and vanishing on-site number fluctuations, which in the atomic limit of the Hubbard model signify the presence of incompressible Mott domains [23]. For both density profiles and atom number
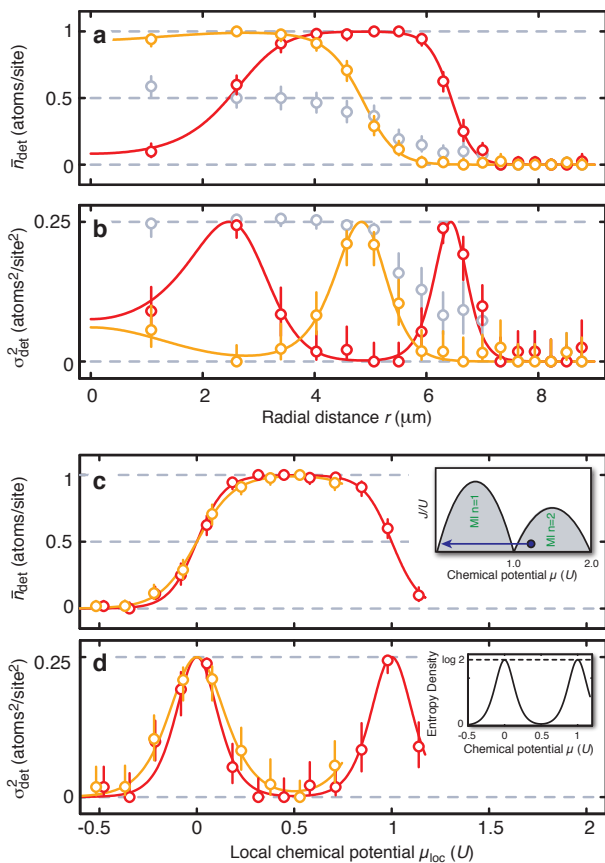
FIG. 4: **Radial atom density and variance profiles.** Radial profiles were obtained from the digitized reconstructed images by azimuthal averaging. **a, b**, Yellow and red points correspond to the $n = 1$ and $n = 2$ MI images of Fig. 2d,e. The grey points were obtained from a BEC (data from Fig. 2a) for reference. The displayed statistical errors are Clopper-Pearson 68% confidence intervals for the binomially distributed number of excitations. For the MIs both density and variance profiles are fitted simultaneously with the model functions of Eqs. (1) and (2) (see Methods) with T, μ and $r_0^2 = 2U/(m\omega_x\omega_y)$ as free parameters. For the two curves, the fits yielded temperatures $T = 0.090(5)U/k_B$ and $T = 0.074(5)U/k_B$, chemical potentials $\mu = 0.73(3)U$ and $\mu = 1.17(1)U$, and radii $r_0 = 5.7(1)\,\mu$m and $r_0 = 5.95(4)\,\mu$m respectively. From the fitted values of T, μ and r_0, we determined the atom numbers of the system to $N = 300(20)$ and $N = 610(20)$. **c, d**, The same data plotted versus the local chemical potential using the local-density approximation. The inset of **c** is a Bose-Hubbard phase diagram ($T = 0$) showing the transition between the characteristic MI lobes and the superfluid region. The line starting at the maximum chemical potential μ shows the part of the phase diagram existing simultaneously at different radii in the trap due to the external harmonic confinement. The inset of **d** is the entropy density calculated for the displayed $n = 2$ MI.

variances we find excellent agreement between the experimental data and the theoretical model for all radial distances. This supports the assumption that our system

is in global thermal equilibrium, in contrast to Ref. [26]. The extracted temperatures of $T = 0.090(5)U/k_B$ and $T = 0.074(5)U/k_B$ for the $n = 1$ and $n = 2$ data are well below the MI melting temperature T_m. Our temperature estimates are conservative since all defects are attributed to thermal excitations in our model. However, defects might also arise due to "collateral damage" caused by atoms undergoing the light-induced collisions. For reference, we show the corresponding data obtained by freezing out the atom distribution of a BEC. We observe the expected saturation of $\bar{n}_{\text{det}}$ at 0.5 together with a maximum variance of σ_{det}^2 at 0.25. We note that the thermal shells surrounding a MI core also exhibit this maximum variance and can be as narrow as 1-2 lattice sites. In Fig. 4c,d we plot both MI data sets versus local chemical potential. In a single image, we thus mapped out an entire line in the phase diagram as illustrated in the inset of Fig. 4c. The slightly different temperatures of the two MIs are clearly visible in the different widths of the variance curves.

Our measurements also confirm with unprecedented clarity that the entropy of the strongly correlated quantum gas is concentrated around the Mott insulating regions, whereas in the center of a MI, for local chemical potentials of $\mu_{\text{loc}} = (n + 1/2)U$, number fluctuations are completely suppressed and the entropy density is essentially zero. For the lowest observed temperature of $T = 0.074(5)U/k_B$ we calculate a 99.7(1)% probability for unity occupation in the center of the $n = 1$ Mott-insulating plateau. Using the zero-tunneling model we can also extract the total entropy per particle for our system $S/(Nk_B) = 0.34(2)$ (see Methods) which is around the critical entropy for quantum magnetism [27].

Finally, we show how a Mott insulator melts, as the temperature (or entropy) of the quantum gas is increased (see Fig. 5). At constant total chemical potential but increasing temperatures, one observes that the Mott domains gradually vanish. Although there is no sharp transition to a normal fluid state in this case, Mott plateaus and number squeezing degrade rapidly, once $T \gtrsim T_m$ (see Figs. 5d,e), as predicted in Ref. [17].

In summary, we have demonstrated single-site and single-particle resolved detection of a strongly correlated system in an optical lattice. Our method can be extended to investigate quantum critical phenomena, density-density correlations or even non-local string-operators that are inaccessible in condensed matter experiments. Our imaging system can be used to focus an off-resonant laser beam onto a single atom and thereby allow single-site manipulation of the atomic qubits [28]. This opens a new avenue for experiments with ultracold quantum gases, where e.g. novel cooling schemes may be applied by accessing regions of high entropy [29]. For future work it would be interesting to investigate how entropy propagates in strongly correlated systems, after injecting it on a local scale into the system. Atoms in the MI with one atom per lattice site are also very promising as a quantum register for scalable quantum computing,
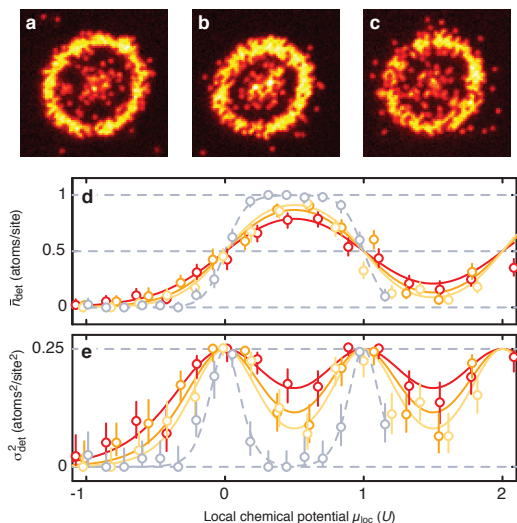
FIG. 5: **Melting of a Mott Insulator.** **a-c** Strongly correlated atomic samples for three different temperatures, and constant total chemical potentials in the zero-tunneling limit. For higher temperatures, an increased number of independent particles or holes appear. Data shown was binned 2x2. **e, f**, Density and variance profiles as a function of chemical potential, determined as described in the caption of Fig. 4. Red, orange and yellow points correspond to the datasets from **a**, **b**, and **c**, respectively. Light blue points correspond to the low-temperature $n = 2$ MI of Fig. 2e and Fig. 4 with $T = 0.074(5)U/k_B$ and $\mu = 1.17(1)U$. The parameters extracted from the radial fits are $T = 0.17(1)U/k_B$, $\mu = 2.08(4)U/k_B$, for **a**, $T = 0.20(2)U/k_B$, $\mu = 2.10(5)U/k_B$, for **b** and $T = 0.25(2)U/k_B$, $\mu = 2.06(7)U/k_B$, for **c**.

especially with the very low defect density shown in this work.

Methods

Preparation of a single 2D system. We started by loading atoms from a magnetic quadrupole trap into a single beam optical dipole trap (1064 nm, beam waist $w_0 = 40\,\mu$m). By translating the focus of the dipole trap using mirrors on a motorized micrometer stage, the atoms were transported in front of the high resolution imaging system within 2.5 s. A magnetic quadrupole field whose center is shifted below the trap compressed the cloud in the axial direction of the dipole trap laser beam. After 500 ms of evaporative cooling in this hybrid trap configuration, we transferred the atoms into the z-lattice. It is oriented along the optical axis of the imaging sys-

tem, parallel to gravity, and superimposed with the hybrid trap. Initially we populated 60 antinodes (slices) of the standing wave, creating independent 2D systems. To extract a single 2D system, we used position dependent microwave transfer in a magnetic field gradient. The gradient with $\partial B/\partial z = 24\,$G/cm (together with a bias field of 32 G) was produced with a single coil placed 50 mm above the atoms; the coil axis coincides with the z-lattice beam. Our magnetic field gradient results in a position dependent frequency shift $\partial\nu/\partial z \sim 5$ kHz/μm of the $|F = 1, m_F = -1\rangle \leftrightarrow |F = 2, m_F = -2\rangle$ transition. An initial microwave frequency sweep over 1 MHz brought all atoms from $|F = 1, m_F = -1\rangle$ to $|F = 2, m_F = -2\rangle$. We then transferred atoms from one slice back to the $|F = 1, m_F = -1\rangle$ state using a resonant Blackman pulse of 5 ms duration. All atoms remaining in $F = 2$ were removed from the trap by a laser pulse resonant with the $F = 2 \rightarrow F' = 3$ transition. We then evaporatively cooled the atoms by ramping down the intensity of the z-lattice from $300\,E_r$ to $\sim 25\,E_r$ within 1.5 s, while simultaneously tilting the potential along the horizontal direction with a magnetic field gradient [30]. Depending on the end point of this evaporation, we created BECs with atom numbers ranging from $50 - 2000$.

Imaging single atoms in the lattice. Our microscope objective was custom made (Leica Microsystems) and is located outside of the vacuum chamber with a working distance of 13 mm. We detected the atoms by illuminating them with an optical molasses, red detuned with respect to the free space resonance by 45 MHz. It consists of two pairs of retroreflected laser beams superimposed with the horizontal lattice axes. A third z-molasses laser beam aligned in reverse direction through the imaging system provided cooling in the vertical direction. The total scattering rate from all laser beams was $\sim 60\,$kHz. With our total detection efficiency of ~ 9 % (solid angle 15%, transmission of all optical elements 71%, camera quantum efficiency 85%), we collect about 5000 photons/atom within our illumination time of 900 ms. To ensure a homogeneous illumination of all atoms, we scanned the retro-reflecting mirrors of the horizontal molasses beams (at a frequency of 300 Hz and 400 Hz) using piezo elements and mutually detuned the molasses beams by 43 Hz. Additionally, we spatially scanned the z-molasses beam across the cloud at a frequency of 100 Hz and an amplitude of 35 μm. We also corrected for an etaloning effect of the CCD camera, which caused a spatially dependent signal strength. We carefully optimized the molasses parameters to minimize hopping of the atoms to adjacent lattice sites, by taking two consecutive images of the same cloud for the first 400 ms and the last 400 ms of our 900 ms illumination period. From the analysis of several of these double images, we found that about 0.5% of the atoms hop during the molasses illumination. Before switching on the molasses, we removed the atoms in the doubly occupied sites with a 50 ms pulse on the $F = 2$ to $F' = 3$ transition, which is 6.8 GHz red detuned for the atoms in $F = 1$,

but efficiently excites into the molecular potentials.

For the horizontal optical lattice laser beams we used two single mode fiber amplifiers seeded with the same narrowband solid-state laser, whereas the vertical lattice beam was derived from an independent solid-state laser. The horizontal axes were mutually detuned by 220 MHz and had orthogonal polarizations. We obtained about 10 W per lattice axis at the experiment, yielding trap depths of about 300 μK.

Reconstruction of the atom number distribution. We developed a deconvolution algorithm to reconstruct the atom number distribution from a fluorescence image. It uses a model of the point spread function (PSF) of our imaging system that was determined from averaging over many images of isolated individual atoms (see Supplementary Information). The algorithm tries different model-configurations for each lattice site and its nearest neighbors in order to minimize the difference of the original image with the reconstructed one. This reconstructed image was obtained by convoluting the atom number distribution with our PSF (see centre row of Fig. 2). The algorithm allows for a variance of the fluorescence level of each atom within $\pm 20\%$ of the mean photon counts. These varying fluorescence levels partially arise from the inhomogeneous intensity of the molasses light. We additionally found an increased fluorescence level of about 10%-20% in the center of very dense $n = 1$ shells of a MI, compared with the isolated atoms in the outer part of the images. This effect might arise from the partial coherence of the light scattered by the atoms, combined with their regular distribution in the lattice.

We have evaluated the fidelity of the reconstruction algorithm by creating simulated images of a known atom distribution using the PSF of our imaging system, the poissonian and superpoissonian noise contributions of the light hitting the EMCCD camera (including the amplification process), and the site-to-site fluorescence fluctuations of $\pm 20\%$. Running the reconstruction algorithm over several hundred of such randomly generated images of MIs at finite temperatures, we find a reconstruction fidelity of $\sim 99.5\%$. In our experiment, the main limitations of the fidelity are atom losses during the detection process due to collisions with background gas atoms. We measured that about 1% of the atoms are lost during the 900 ms detection period, which corresponds to a trap lifetime of ~ 75 s.

Radial atom number distribution and variance. In the zero-tunneling regime (the "atomic limit" of a MI), the atom number distribution at a lattice site at radius r is given by $P_r(n) = e^{\beta[\mu_{\text{loc}}(r)n - E_n]}/Z(r)$, where $Z(r) = \sum_n e^{\beta[\mu_{\text{loc}}(r)n - E_n]}$ is the grand canonical partition function, $\beta = 1/(k_B T)$, $\mu_{\text{loc}}(r)$ the local chemical potential and $E_n = Un(n-1)/2$ is the interaction energy. Using a local density approximation (LDA), we define μ_{loc} in terms of the global chemical potential μ and the external harmonic trapping confinement: $\mu_{\text{loc}}(r) = \mu - \frac{1}{2}m(\omega_x^2 x^2 + \omega_y^2 y^2)$. Taking the light induced losses into account we calculate the expected detected density at different radii:

$$\bar{n}_{\text{det}}(r) = \frac{1}{Z(r)} \sum_n \text{mod}_2(n) e^{\beta[\mu_{\text{loc}}(r)n - E_n]} \tag{1}$$

In the presence of light induced collisions $\overline{n_{\text{det}}^2}(r) = \bar{n}_{\text{det}}(r)$ and the detected variance is therefore simply

$$\sigma_{\text{det}}^2(r) = \bar{n}_{\text{det}}(r) - \bar{n}_{\text{det}}^2(r). \tag{2}$$

We extracted radial density and variance profiles from the reconstructed two-dimensional atom distribution of a single image. For this, we first determined the center of the cloud, and then binned the lattice sites according to their distance from the center, thereby correcting for the ellipticity of 10%. The bin sizes were chosen larger near the center to have sufficient statistics.

We fitted the experimental profiles to Eqns. (1) and (2) and extracted the temperature and the global chemical potential. These can then be used to calculate the original atom number distribution $P_r(n)$. Inserting the radius corresponding to $\mu_{\text{loc}} = 0.5$ we extract the maximal theoretical unity occupation probability. We can furthermore calculate the local entropy density $S_{\text{loc}}(r) = -k_B \sum_n P_r(n) \ln[P_r(n)]$. Summing the density and entropy density over the lattice sites we calculate the total number of particles $N = 591(9)$ and the total entropy $S/k_B = 200(13)$ given the fitted values of T and μ from the $n = 2$ data of Fig. 4. This gives the entropy per particle $S/(Nk_B) = 0.34(2)$.

[1] Fisher, M. P. A., Weichman, P. B., Grinstein, G. & Fisher, D. S. Boson localization and the superfluid-insulator transition. *Phys. Rev. B* **40**, 546–570 (1989).

[2] Jaksch, D., Bruder, C., Cirac, J. I., Gardiner, C. & Zoller, P. Cold bosonic atoms in optical lattices. *Phys. Rev. Lett.* **81**, 3108–3111 (1998).

[3] Greiner, M., Mandel, M., Esslinger, T., Hänsch, T. & Bloch, I. Quantum phase transition from a superfluid to a Mott insulator in a gas of ultracold atoms. *Nature* **415**, 39–44 (2002).

[4] Spielman, I. B., Phillips, W. D. & Porto, J. V. Mott-Insulator Transition in a Two-Dimensional Atomic Bose Gas. *Phys. Rev. Lett.* **98**, 080404 (2007).

[5] Paredes, B. *et al.* Tonks-Girardeau gas of ultracold atoms in an optical lattice. *Nature* **429**, 277–281 (2004).

[6] Kinoshita, T., Wenger, T. & Weiss, D. S. Observation of a one-dimensional Tonks-Girardeau gas. *Science* **305**, 1125–1128 (2004).

[7] Jördens, R., Strohmaier, N., Günter, K., Moritz, H. & Esslinger, T. A Mott insulator of fermionic atoms in an

optical lattice. *Nature* **455**, 204–207 (2008).

[8] Schneider, U. *et al.* Metallic and Insulating Phases of Repulsively Interacting Fermions in a 3D Optical Lattice. *Science* **322**, 1520–1525 (2008).

[9] Gerbier, F., Fölling, S., Widera, A., Mandel, O. & Bloch, I. Probing Number Squeezing of Ultracold Atoms across the Superfluid-Mott Insulator Transition. *Phys. Rev. Lett.* **96**, 090401 (2006).

[10] Raussendorf, R. & Briegel, H. J. A One-Way Quantum Computer. *Phys. Rev. Lett.* **86**, 5188–5191 (2001).

[11] Nelson, K. D., Li, X. & Weiss, D. S. Imaging single atoms in a three-dimensional array. *Nature Phys.* **3**, 556–560 (2007).

[12] Gericke, T., Würtz, P., Reitz, D., Langen, T. & Ott, H. High-resolution scanning electron microscopy of an ultracold quantum gas. *Nature Phys.* **4**, 949–953 (2008).

[13] Gemelke, N., Zhang, X., Hung, C.-L. & Chin, C. In situ observation of incompressible Mott-insulating domains in ultracold atomic gases. *Nature* **460**, 995–998 (2009).

[14] Karski, M. *et al.* Nearest-Neighbor Detection of Atoms in a 1D Optical Lattice by Fluorescence Imaging. *Phys. Rev. Lett.* **102**, 053001 (2009).

[15] Bakr, W. S., Gillen, J. I., Peng, A., Fölling, S. & Greiner, M. A quantum gas microscope for detecting single atoms in a Hubbard-regime optical lattice. *Nature* **462**, 74–77 (2009).

[16] Bakr, W. S. *et al.* Probing the Superfluid-to-Mott Insulator-Transition at the Single-Atom Level. *10.1126/science.1192368* (2010).

[17] Gerbier, F. Boson Mott Insulators at Finite Temperatures. *Phys. Rev. Lett.* **99**, 120405 (2007).

[18] Ho, T.-L. & Zhou, Q. Intrinsic Heating and Cooling in Adiabatic Processes for Bosons in Optical Lattices. *Phys. Rev. Lett.* **99**, 120404 (2007).

[19] DePue, M. T., McCormick, C., Winoto, S. L., Oliver, S. & Weiss, D. S. Unity Occupation of Sites in a 3D Optical Lattice. *Phys. Rev. Lett.* **82**, 2262–2265 (1999).

[20] Jaksch, D. & Zoller, P. The cold atoms Hubbard toolbox. *Ann. Phys.* **315**, 52–79 (2005).

[21] Bloch, I., Dalibard, J. & Zwerger, W. Many-body physics with ultracold gases. *Rev. Mod. Phys.* **80**, 885–964 (2008).

[22] Krauth, W. & Trivedi, N. Mott and Superfluid Transitions in a Strongly Interacting Lattice Boson System. *Europhys. Lett.* **14**, 627–632 (1991).

[23] Rigol, M., Batrouni, G. G., Rousseau, V. G. & Scalettar, R. T. State diagrams for harmonically trapped bosons in optical lattices. *Phys. Rev. A* **79**, 053605 (2009).

[24] Fölling, S., Widera, A., Müller, T., Gerbier, F. & Bloch, I. Formation of Spatial Shell Structure in the Superfluid to Mott Insulator Transition. *Phys. Rev. Lett.* **97**, 060403 (2006).

[25] Campbell, G. K. *et al.* Imaging the Mott Insulator Shells by Using Atomic Clock Shifts. *Science* **313**, 649–652 (2006).

[26] Hung, C.-L., Zhang, X., Gemelke, N. & Chin, C. Slow Mass Transport and Statistical Evolution of an Atomic Gas across the Superfluid-Mott-Insulator Transition. *Phys. Rev. Lett.* **104**, 160403 (2010).

[27] Capogrosso-Sansone, B., Söyler, S. G., Prokofev, N. V. & Svistunov, B. V. Critical entropies for magnetic ordering in bosonic mixtures on a lattice. *Phys. Rev. A* **81**, 053622 (2010).

[28] Zhang, C., Rolston, S. L. & Das Sarma, S. Manipulation of single neutral atoms in optical lattices. *Phys. Rev. A* **74**, 042316 (2006).

[29] Bernier, J.-S. *et al.* Cooling fermionic atoms in optical lattices by shaping the confinement. *Phys. Rev. A* **79**, 061601(R) (2009).

[30] Hung, C.-L., Zhang, X., Gemelke, N. & Chin, C. Accelerating evaporative cooling of atoms into Bose-Einstein condensation in optical traps. *Phys. Rev. A* **78**, 011604 (2008).

Supplementary Information

Determination of lattice angles and spacing. To characterize our imaging system and to determine the lattice structure, we used a fluorescence image of a dilute thermal could, similar to the inset in Fig. 1 of the main text. The lattice axes are oriented at approximately $\pm 45°$ with respect to our images. A precise determination of this angle and the lattice spacing is needed so that the deconvolution algorithm works with high fidelity. We first determined the center positions of isolated atoms from this image by a simple fitting algorithm. The histogram of the mutual distances projected in a coordinate system rotated by an angle θ clearly shows the periodicity of the lattice (see Fig. 6a,b) and the visibility of the pattern depends very sensitively on θ. For a quantitative analysis, we fit a sum of equidistant Gaussians to the histogram. The width of the Gaussians for different values of θ (Fig. 6c) shows a clear minimum at $\theta = 45.85(1)°$. We obtained a similar graph for the other lattice axis and found an angle of $-45.55(1)°$. The distance of the Gaussians is 4.269(4) pixel which corresponds to lattice period of 532 nm. Thus, our magnification factor is 128.4(2) and
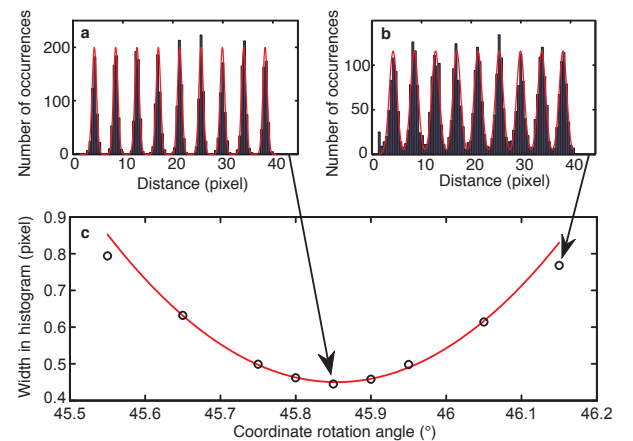

FIG. 6: **Determination of the lattice angles**. **a,b** Histogram of the distances between the center positions of individual atoms projected in a coordinate system rotated by an angle θ. The line is a fit to a sum of equidistant Gaussians. **c** The width of the fitted Gaussians show a clear minimum. The red line is a parabolic fit and yields a minimum rotation angle at $\theta = 45.85(1)°$.
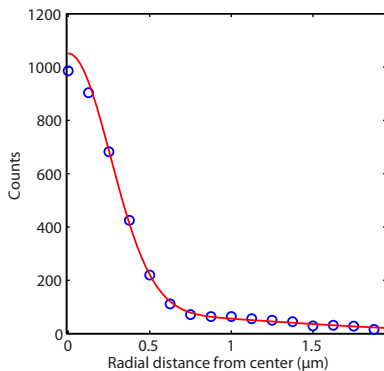
FIG. 7: **Azimuthal average of our experimentally obtained point spread function.** The data was obtained by averaging over 68 signals of single atoms. The line is a fit with the double Gaussian of Eq. (3) and yields $\sigma_1 = 2.06(5)$ pixels, $\sigma_2 = 9.6(1.2)$ pixels, $a = 0.075(2)$ and $C = 1050(7)$.

one pixel of the CCD camera corresponds to 124.6(1) nm in the object plane. The angles and lattice spacing determined by this method are used as fixed parameters for our deconvolution algorithm. We also found that the phases of the two lattice axes slightly drift from shot to shot. They are determined for each image by fitting the center positions of single atoms in the outer part of the images.

Determination of the point spread function. We determined our point spread function (PSF) from the fluorescence image of a dilute atomic cloud. We summed the fluorescence image of many individual atoms that were isolated from their neighbors by more that 12 pix-

els. The summed image is almost radially symmetric and we computed an azimuthal average (see Fig. 7). We expect our PSF to be a convolution of an Airy disk with a Gaussian, taking into account fluctuations of the lattice with respect to the imaging system and the width of the atomic wavepacket in the potential wells. Due to this convolution, the first minimum of the airy pattern is not visible in our averaged signal. We found that our PSF can be well approximated by a double Gaussian:

$$
\begin{aligned}
PSF(x,y) \;=\; & C\left[(1-a)\exp\left(-0.5(x^2+y^2)/\sigma_1^2\right)\right. \\
& \left.+\; a\exp\left(-0.5(x^2+y^2)/\sigma_2^2\right)\right]
\end{aligned}
\tag{3}
$$

with widths σ_1, σ_2 and a parameter a describing the relative amplitudes. The maximum fluorescence level C varies from day to day and is in the range of 800-1200 counts.

Single-band Hubbard parameters

For a z-lattice depth of $V_z = 26E_r$, the single-band Hubbard parameters for our 2D system are given in the following table:

$V_{x,y}(E_r)$	J/h (Hz)	U/h (Hz)
5	134	382
10	39	607
15	13	776
20	5	917
25	2	1039

Note that one expects the the single-band Hubbard parameters to be slightly renormalized due to multi-orbital effects.